Optimization of direct extrusion process for Nd-Fe-B magnets using active learning assisted by machine learning and Bayesian optimization

G. Lambard [a,*], T.T. Sasaki [b], K. Sodeyama [a], T. Ohkubo [b], K. Hono [b]

[a] *Energy Materials Design Group, Research and Services Division of Materials Data and Integrated System (MaDIS), National Institute for Materials Science (NIMS), Tsukuba, Japan*
[b] *Elements Strategy Initiative Center for Magnetic Materials (ESICMM), National Institute for Materials Science (NIMS), Tsukuba, Japan*

ARTICLE INFO

ABSTRACT

Process optimization of permanent magnet is time-consuming as the microstructure that depends on alloy compositions and process parameters must be optimized to achieve high coercivity. Given a raw material of fixed composition, the optimization of process involves the refinement of grains size, the alignment of crystallographic orientation and the formation of intergranular phase. In this paper, we implemented an active learning pipeline assisted by machine learning and Bayesian optimization (ALMLBO) for predicting magnetic properties from process parameters and propose optimum conditions leading to high coercivity and remanence in Nd-Fe-B anisotropic magnets fabricated by direct hot extrusion. ALMLBO allowed us to optimize the process to exhibit high coercivity, $\mu_0 H_c$−1.7 T, and remanence, $\mu_0 B_r$−1.4 T, simultaneously, resulting in an excellent maximum energy product, $(BH)_{max}$−380 kJ/m^3. We show that an ALMLBO pipeline is an effective tool for optimizing process for Nd-Fe-B anisotropic magnets.

Nd-Fe-B permanent magnets for electric vehicle traction motors and wind turbines gain satisfactory coercive force at their operating temperatures of ∼ 160 °C by partially substituting Nd with heavy rare earth elements (HRE) such as Dy and Tb in the $Nd_2Fe_{14}B$ phase. Recently, there is a strong demand to achieve high coercivity ($\mu_0 H_c$) without alloying HREs because of their scarcity and high cost [1,2]. Several approaches have been proposed to increase $\mu_0 H_c$, e.g. the formation of (non-ferromagnetic) Nd-rich intergranular phases [3–5], HRE grain boundary diffusion process [6,7] and grain refinement [8–10] have been demonstrated in sintered magnets. The grain refinement is effective to increase the coercivity as it leads to the reduction of the stray field from neighboring grains, and the temperature coefficient of coercivity is also improved [11]. Hot deformation of melt-spun ribbons induces a large anisotropic microstructure with platelet-shaped ultrafine-grained magnets [12,13]. Because the average grain size in the hot-deformed magnets is about several hundreds of nanometer, which is more than an order of magnitude smaller than in sintered magnets (∼ 3 μm), they are expected to exhibit superior coercivity and its thermal stability compared to the sintered magnets [14]. The

hot deformation process consists of a hot pressing for obtaining a consolidated bulk and following hot deformation process, such as die-upsetting [13], backward extrusion [15], and direct extrusion [14], to develop a strongly textured grain structure. To date, most of the studies on hot-deformed magnets have been performed for die-upset process to realize excellent permanent magnet properties by optimizing the composition [16–20] and the process parameters [20–24]. Recently, large plate-shaped hot-deformed magnets fabricated by the direct extrusion process are adopted in traction motors for hybrid vehicles [25]. However, there are few reports on the evolution of microstructure and resulting magnetic properties on directly extruded magnets. As the size of the extruded magnets are relatively large compared to the die-upset magnets, various process parameters must be optimized to achieve good permanent magnet properties throughout the relatively large plates. In this paper, we adopted an active learning pipeline assisted by machine learning and Bayesian optimization (ALMLBO) to this end.

Active learning is a general framework which includes the "learning" step formed from past experiments and a set of actions resulting from the experimental feedbacks, the "active" step. Many learning-acting cycles form an active learning pipeline. One may note that a trial-and-error method follows an active learning scheme if an update in the theoretical/empirical knowledge and a forward action, modifying an experimental design to fulfill an

Table 1

List of tunable process parameters $\theta_i \in \theta_i$, issued from $\theta = \{HP_T, HP_L, HE_T, HE_{RS}, HE_{LL}, Die_{ID}\}$, with their accessible domain d_i and resolution δd_i chosen for the hot extrusion of Nd-Fe-B permanent magnets. HP_T and HP_L are the hot-press temperature and load, respectively. HE_T, HE_{RS} and HE_{LL} are the hot extrusion temperature, ram speed, and load limit, respectively. Die_{ID} is the identification number of a die of a given shape used at the extrusion exit.

Process parameter θ_i	Domain d_i	Resolution δd_i
HP_T	[500,800] °C	25 °C
HP_L	[50,700] kN	10 kN
HE_T	[750,900] °C	25 °C
HE_{RS}	[0.1,10] mm.s^{-1}	0.1 mm.s^{-1}
HE_{LL}	[10,100] kN	10 kN
Die_{ID}	[0,10]	1

objective, are performed at each cycle. However, a systematic and cyclic update may be hard especially if the objective is non-linearly linked to a large number of experimental parameters. In this sense, an ALMLBO pipeline offers the possibility to optimize salient input features among 6 experimentally tunable process parameters for achieving high $\mu_0 H_c$, remanence ($\mu_0 B_r$), and squareness ($Sq.$), summarized into a high maximum energy product ($(BH)_{max}$), in hot-extruded magnets. Here, we report a highest class of magnetic properties ($\mu_0 H_c \sim 1.70$ T, $\mu_0 B_r \sim 1.40$ T, $Sq. \sim 99\%$, and $(BH)_{max} \sim 380$ kJ/m^3) in a scaled-up plate-shaped ($30 \times 5 \times 70$ mm^3) anisotropic permanent magnet fabricated by hot extrusion after just 3 cycles of ALMLBO using commercial $Nd_{14}Fe_{76}Co_{3.4}B_6Ga_{0.6}$ (at%) powder (MQU-F^{TM}).

First, we defined a fixed protocol for building our dataset composed of the magnetic properties $\Pi = \{\mu_0 H_c, \mu_0 B_r, Sq.\}$ with their $(BH)_{max}$, and tunable process parameters $\theta = \{HP_T, HP_L, HE_T, HE_{RS}, HE_{LL}, Die_{ID}\}$ of hot-extruded Nd-Fe-B magnets, where: HP_T and HP_L are the temperature and the load for hot pressing, respectively; HE_T, HE_{RS} and HE_{LL} are the hot extrusion temperature, ram speed, and load limit, respectively; Die_{ID} is the identification number of a die of a given shape used at the extrusion exit. We used commercial MQU-F^{TM} melt-spun flakes with the nominal composition of $Nd_{14}Fe_{76}Co_{3.4}B_6Ga_{0.6}$ (at%). These flakes were consolidated into a bulk under uniaxial hot-press followed by a direct extrusion process to obtain an extruded magnet with a size of ~ 30 mm in width, 5–7 mm in thickness, and ~ 70 mm in length, at various hot pressing and extrusion conditions θ. Extrusions were then cut into cuboidal shapes with 6 mm in width, 6 mm in thickness, and 5–8 mm in height for measuring the magnetic properties Π, and $(BH)_{max}$, using a B-H tracer (Tamakawa Co., Ltd, TM-BH25-C1) at room temperature. A microstructure analysis was performed by scanning electron microscope (SEM). The SEM analysis was performed using a Carl Zeiss Crossbeam 1540 EsB FIB/SEM. Specimens for the SEM analysis were prepared by a mechanical polishing followed by a surface cleaning by focused ion beam (FIB) to remove surface contamination.

The ALMLBO pipeline was kickstarted with only $n = 18$ samples $\{\theta_i, \Pi_i \mid i = 1,...,18\}$, initially selected on a trial-and-error basis to obtain crack-free hot-extruded samples with satisfactory magnetic properties Π, each Π_i being identified as a set of average values $\{\overline{\mu_0 H_c}, \overline{\mu_0 B_r}, \overline{Sq.}\}$ calculated from m magnetically characterized cuboids, extracted from the same extruded parent sample, m varying from 1 to 25 depending on the parent sample. Each tunable process parameter $\theta_i \in \theta_i$, issued from all possible θ, was restricted to vary within a domain d_i with a resolution δd_i, both chosen to be experimentally feasible, as summarized in Table 1. At this stage, more than 66 million combinations of θ_i were experimentally possible.

Then, a cycle of the ALMLBO pipeline, summarized in Fig. 1(a), is conducted as follows: (i) a set ε_{RF} of 3 ensembles of n_{RF} Random Forests (RF) [26] regressors, with $n_{RF} = n$ available experi-

mental samples and default hyper-parameters of the RF models assigned as in [27], are trained to uniquely predict each property in Π_i following a leave-one-out [28] cross-validation scheme, and using a mean-squared-error as the loss function to minimize during training. For conciseness, a comparison between predicted and observed values for the average $(BH)_{max}$ (kJ/m^3) only is shown here in Fig. 1(b) before using ALMLBO (gray squares), and after 3 cycles of ALMLBO (blue, red, and green squares, respectively). For a detailed visualization of the individual prediction performance on the properties Π, **Fig. S1** in the supplementary materials can be examined. Overall, a reasonable average root-mean-square-error (RMSE) $\sim 17.2 \pm 13.8$ kJ/m^3 on the $(BH)_{max}$ is achieved. Furthermore, salient parameters $\theta_s = \{HE_T, HE_{LL}, Die_{ID}\}$ for predicting Π properties were identified according to their variable importance as shown in Fig. 2(a) [26]. Later on, parameters in θ_s are kept for optimization, and the remaining parameters $\theta \not\subset \theta_s$ are tuned to their most efficient values during experimental processing. This sole reduction of tunable process parameters from θ to θ_s for optimization purpose induced a sharp decrease in experimentally possible θ_i conditions to only 770, i.e. roughly 5 orders of magnitude lower than before the filtering of θ over saliency. Also, it is worth noting that θ_s did not change with further data integration after each ALMLBO cycle; (ii) A set $\{\theta_s, \Pi\}|_r$ of 100 samples, with $\theta_{s,i} \in d_i$ (see Table 1) for the ith sample, is randomly evaluated through ε_{RF} to initialize a following Gaussian process regressor at step (iii), and relax from any experimental biases and/or local optima that would have occurred during the preparation of the dataset issued from a previous cycle; (iii) A Gaussian process is trained on $\{\theta_s, \Pi\}|_r$ that serves as a surrogate function S to exploit and explore θ_s; (iv) A set θ_s* of 10 samples that maximizes the expected improvement [29], built over the product $\mu_0 H_c \times \mu_0 B_r \times Sq.$ and chosen as acquisition function, is proposed for experimental feedback. Steps (ii), (iii) represents the Bayesian optimization part in the ALMLBO pipeline here; (iv) θ_s* is experimentally evaluated and corresponding $\Pi*$ properties are reported. If $\Pi*$ are judged high enough, the ALMLBO pipeline is stopped, otherwise another cycle (i)–(iv) is started by adding newly acquired experimental data to the whole dataset.

Fig. 2(b) shows the evolution of $(BH)_{max}$ (kJ/m^3) successfully acquired with a B–H tracer before (gray squares) and during 3 cycles of ALMLBO (blue, red, and green squares, respectively). It is worth noting that, before ALMLBO pipeline was initiated, the improvement in $(BH)_{max}$ had reached a plateau which was hard to overcome without ALMLBO. This is essentially because of the number of involved process parameters θ, as well as their non-linear relationship to Π properties, that rendered difficult the possibility to intuit a θ-to-Π relationship without assistance from the ALMLBO pipeline.

Fig. 3(a) shows the relationship between $\mu_0 H_c$ (T) and $(BH)_{max}$ (kJ/m^3) obtained from extruded samples in a series of extrusion experiments and various hot-deformed samples fabricated by die-upsetting process [19,20,37–39,23,30–36]. gray and colored squares (blue, red, and green) indicate experimental data acquired before and after the use of the ALMLBO pipeline, respectively. Before using an ALMLBO, high $\mu_0 H_c$ and $(BH)_{max}$ were difficult to achieve simultaneously. However, the ALMLBO was effective at solving this issue, leading to the realization of high $\mu_0 H_c$ and $(BH)_{max}$. The extrusion fabricated in the early stage of the experiment without ALMLBO (Sample A in Fig. 3(a)) exhibits a low $\mu_0 H_c \sim 1.2$ T, $\mu_0 B_r \sim 1.2$ T, and $Sq. \sim 95\%$ from process parameters $\theta = \{HP_T \sim 600$ °C, $HP_L \sim 700$ kN, $HE_T \sim 800$ °C, $HERS \sim 1$ mm.s^{-1}, $HE_{LL} \sim 35$ kN, $Die_{ID} = 0\}$, as depicted by its demagnetization curve in Fig. 3(b). The use of a single cycle of ALMLBO leads to a sharp increase in $\mu_0 H_c$, $\mu_0 B_r$ and $Sq.$ to 1.7 T, 1.4 T, and 99%, respectively, from process parameters $\theta = \{HP_T \sim 600$ °C, $HP_L \sim 700$ kN, $HE_T \sim 750$ °C, $HE_{RS} \sim 1$ mm.s^{-1}, $HE_{LL} \sim 50$ kN, $Die_{ID} = 9\}$ resulting in a high $(BH)_{max} \sim 380$ kJ/m^3. It is worth noting that the latter
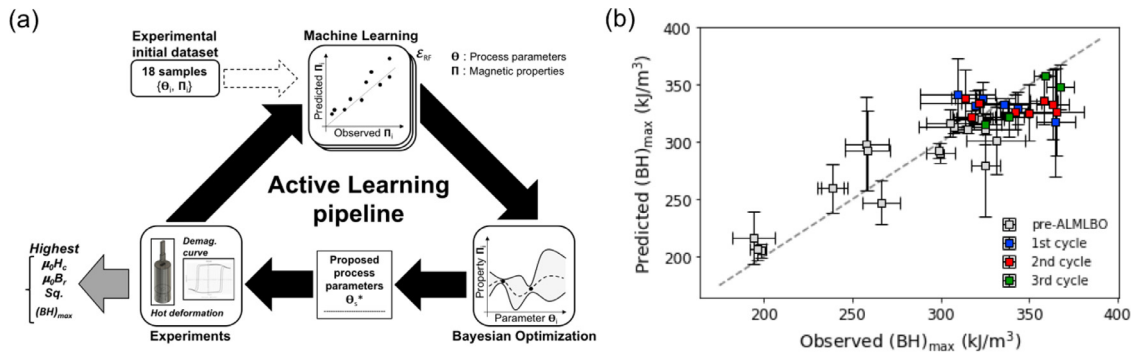
Fig. 1.. (a) Active learning assisted by machine learning and Bayesian optimization (ALMLBO) applied to the optimization of process parameters of hot-deformed Nd-Fe-B magnets for achieving high magnetic properties ($\mu_0 H_c$, $\mu_0 B_r$, Sq., $(BH)_{max}$); (b) Comparison between predicted (Random Forests regression [26]) and observed average maximum energy product $(BH)_{max}$ (kJ/m^3) from a pre-, 1st, 2nd, and 3rd ALMLBO cycle (gray, blue, red, and green squares, respectively) with vertical and horizontal error bars representing a standard deviation related to a leave-one-out [28] cross-validation and computed from m experimental measurements, respectively (the dashed line shows a perfect prediction for the purpose of visual guidance only) (For interpretation of the references to color in this figure, the reader is referred to the web version of this article).
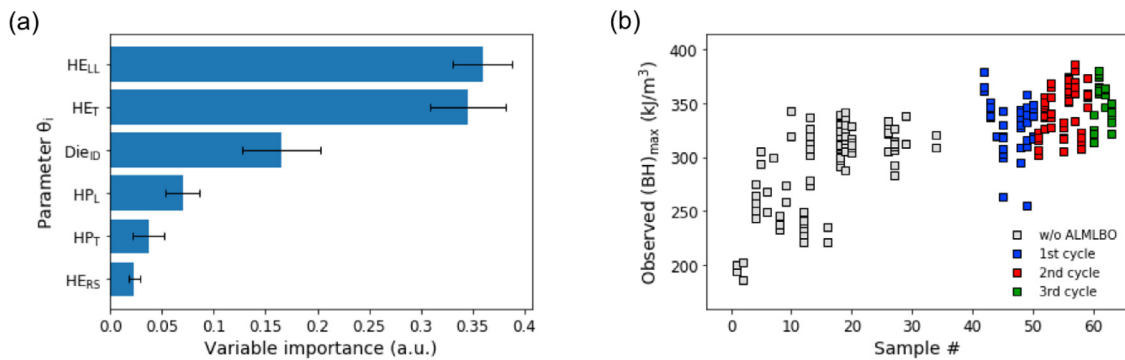

Fig. 2.. (a) Distribution of average variable importance [26] for the process parameters θ_i ranked by saliency order from top to bottom (mean values and error bars are provided according to the leave-one-out [28] cross-validation used for Random Forests [26] models training); (b) Evolution of the maximum energy product, $(BH)_{max}$ (kJ/m^3), calculated from measured {$\mu_0 H_c$, $\mu_0 B_r$, Sq.}, as a function of the sample number (a given sample may possess 1 to 25 series of measurement). Blue, red, and green squares highlight three cycles of ALMLBO, respectively. The gray squares correspond to a data acquirement without ALMLBO, i.e. the initial dataset. (For interpretation of the references to color in this figure, the reader is referred to the web version of this article).
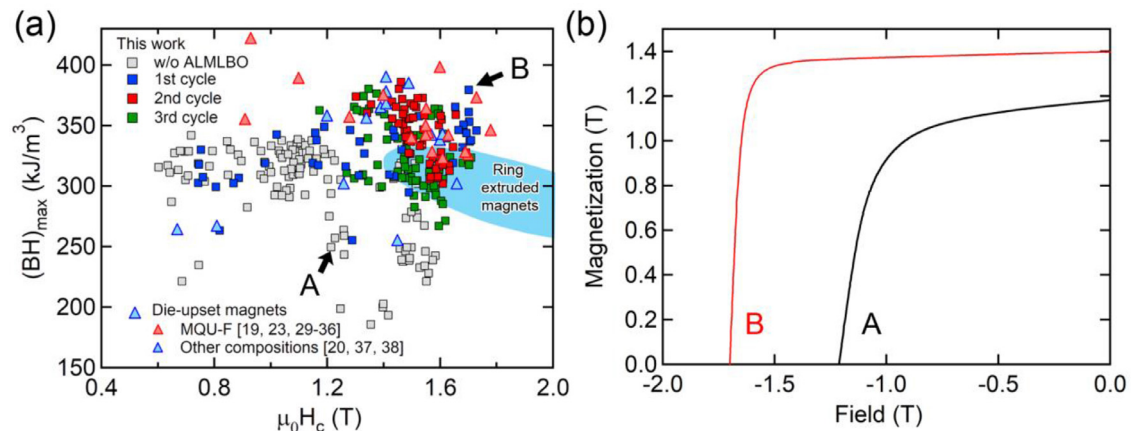

Fig. 3.. (a) Relationship between coercivity, $\mu_0 H_c$ (T), and maximum energy product, $(BH)_{max}$ (kJ/m^3), for extruded samples fabricated during this study and those reported in previous work [19,20,23,30–39]. gray and colored squares (blue, red, and green) indicate data points acquired without and with ALMLBO, respectively; (b) Demagnetization curves for samples A (black) and B (red) indicated with arrows in Fig. 3(a) (For interpretation of the references to color in this figure, the reader is referred to the web version of this article).

achievement is comparable with the highest $\mu_0 H_c$ – $(BH)_{max}$ balance only achieved until now with a hot-deformed magnet of similar composition (MQU-F^{TM}), but fabricated by die-upsetting process [19,23,30–39]. A direct comparison of samples A and B by their respective process parameters θ suggests a directional dependency of $\mu_0 H_c$, $\mu_0 B_r$, Sq., and $(BH)_{max}$ on salient process parameters HE$_T$, and HE$_{LL}$. A decrease in HE$_T$ towards the melting temper-

ature of a consolidated bulk of Nd$_{14}$Fe$_{76}$Co$_{3.4}$B$_6$Ga$_{0.6}$ (at%) flakes (∼730 °C obtained by differential scanning calorimetry), and an increase in HE$_{LL}$, with a careful choice of the die, lead to improved magnetic performance, i.e. increased $\mu_0 H_c$, $\mu_0 B_r$, Sq., and $(BH)_{max}$, and controlled as advanced by the variable importance analysis illustrated in Fig. 2(a). Furthermore, the distributions of $\mu_0 H_c$, $\mu_0 B_r$, Sq., and $(BH)_{max}$ as a function of the process parameters θ, illus-
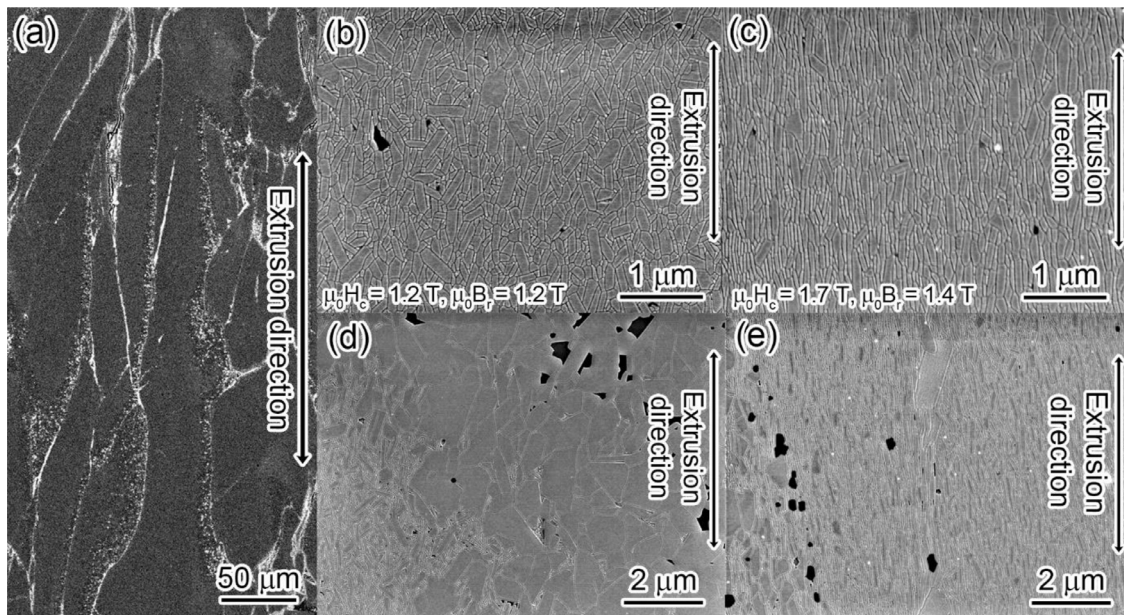
Fig. 4.. (a) Low magnification backscattered electron SEM image of a typical extruded magnet. In-lens secondary electron SEM images of samples with low (b) and high (c) coercivity and remanence obtained from flake interior, and equivalents from low (d) and high (e) coercivity and remanence obtained from an area near flake boundaries.

trated in Figs. S2–S5 of the supplementary materials, respectively, reveal the magnetic properties improvement as a non-linear control inference problem where the de-multiplication of data points at a fixed process parameter shows that magnetic properties are highly multi-parametric, and where the Die_{ID} in sub-figures (f) and, more notably, the HE_{LL} in sub-figures (e) exhibits multiple tendencies.

Fig. 4(a) shows a low-magnification backscattered electron (BSE) SEM image showing a typical microstructure of the center part of extruded magnet. The brightly imaging contrast located near the former flake boundaries are mainly neodymium oxides which were present on the surfaces of MQU-F powder. The flakes were elongated along the extrusion direction. Even though there is no significant difference in the low-magnification microstructure between samples A and B, higher magnification in-lens secondary electron SEM images show different features that might cause the difference in their magnetic properties in Fig. 4.(b)–(e). Inside a flake, platelet-shaped ultra-fine grains with a low volume fraction of Nd-rich phases are present, which are darkly imaged for the $Nd_2Fe_{14}B$ main phase, as seen in Fig. 4(b), (c). First of all, there is a significant difference in the shape of the $Nd_2Fe_{14}B$ grains. The grains in sample B are more elongated and finer than in sample A. The minor and major axes of ellipses delimiting segmented grains are about 90 ± 59 nm (72 nm) and 242 ± 155 nm (195 nm), respectively, for sample A, and 69 ± 172 nm (43 nm) and 554 ± 445 nm (423 nm), respectively, for sample B (characteristics of segmented grains are given as a mean value associated to a standard deviation, with a median value given between parenthesis, here and below). The aspect-ratio is about 2.9 ± 1.3 (2.6) for sample A, and 10.1 ± 5.4 (9.4) for sample B. Furthermore, the longitudinal axes of the $Nd_2Fe_{14}B$ grains, which correspond to the normal axes to the easy axes of the $Nd_2Fe_{14}B$ grains, are strongly aligned for sample B compared to sample A. The orientation with the hot extrusion axis is about 14.4 ± 46.1 ° (-1.6 °) for sample A, and 3.9 ± 9.6 ° (3.1 °) for sample B. Such strong alignment of the $Nd_2Fe_{14}B$ grains led to the high $\mu_0 B_r$ in sample B. Fig. 4(d),(e) show the in-lens secondary SEM images showing the microstructure near the flake boundaries for samples A and B, respectively. Many $Nd_2Fe_{14}B$ coarse grains with ~ 2 μm in diameter are observed around the flake boundaries in sample A, and the ori-

entation of ultra-fine $Nd_2Fe_{14}B$ grains around those coarse grains is rather random (Fig. 4(d)). Unlike sample A, the microstructure of sample B consists of strongly aligned ultra-fine $Nd_2Fe_{14}B$ grains around the flake boundaries while there is a small volume fraction of coarse grains (Fig. 4(e)). These $Nd_2Fe_{14}B$ coarse grains might have caused the low coercivity as these grains are known to be preferential nucleation sites for the reverse domains in the demagnetization process [19,21]. Therefore, the optimization of salient process parameters θ_s led to the development of preferential microstructures which consist of strongly aligned and ultra-fine $Nd_2Fe_{14}B$ grains throughout the bulk for simultaneously achieving high remanence and coercivity, respectively. In this study, the relationship between a microstructure and its permanent magnetic quality in terms of coercivity and remanence is discussed rather qualitatively. However, if the quantitative microstructure-property relationship is later established by thoroughly analyzing a massive dataset of microstructures obtained in a series of extrusion experiments, as in Fig. 3(a), through an extensive image analysis, the design of microstructures for extruded magnets with simultaneously improved coercivity and remanence could be further achieved.

In summary, this study has demonstrated the effectiveness of the ALMLBO in suggesting process parameters for fabricating hot-extruded Nd-Fe-B magnets with excellent permanent magnetic properties from a dataset (18 hot-extruded initial samples) more than six orders of magnitude smaller than the total number of experimentally possible hot processing ($\sim$66 million), and within a fairly short amount of time ($\sim$9 months). The best hot-extruded magnet fabricated using MQU-F powder exhibited high coercivity, $\mu_0 H_c \sim 1.7$ T, remanence, $\mu_0 B_r \sim 1.4$ T, and squareness, $Sq. \sim 99$%, resulting in a high maximum energy product $(BH)_{max} \sim 380$ kJ/m^3 due to the formation of strongly aligned and ultrafine grains structure throughout the bulk.

Research data for this article

[dataset] G. Lambard, T.T. Sasaki, K. Sodeyama, T. Ohkubo, K. Hono, Process parameters and magnetic properties (coercivity, remanence, squareness, maximum energy product) of Nd-Fe-B anisotropic magnets fabricated by direct hot extrusion and driven

by machine learning, Materials Data Repository, NIMS, v1, 2021. https://doi.org/10.1080/27660400.2021.1993729.

Declaration of Competing Interest

Acknowledgments

Supplementary materials

Supplementary material associated with this article can be found, in the online version, at doi:10.1016/j.scriptamat.2021.114341.

References

[1] O. Gutfleisch, M. a Willard, E. Brück, C.H. Chen, S.G. Sankar, J.P. Liu, Adv. Mater. 23 (2011) 821–842.
[2] J.M.D. Coey, Engineering 6 (2020) 119–131.
[3] F. Vial, F. Joly, E. Nevalainen, M. Sagawa, K. Hiraga, K.T. Park, J. Magn. Magn. Mater. 242–245 (2002) 1329–1334.
[4] H. Sepehri-Amin, T. Ohkubo, T. Shima, K. Hono, Acta Mater. 60 (2012) 819–830.
[5] T.T. Sasaki, T. Ohkubo, Y. Takada, T. Sato, A. Kato, Y. Kaneko, K. Hono, Scr. Mater. 113 (2016) 218–221.
[6] K.T. Park, K. Hiraga, M. Sagawa, in: Proceedings of the 16th Workshop Rare-Earth Magnets and Their Applications, Japan Institute of Metals, 2000, pp. 257–264.
[7] K. Hirota, H. Nakamura, T. Minowa, M. Honshima, IEEE Trans. Magn. 42 (2006) 2909–2911.
[8] R. Ramesh, G. Thomas, B.M. Ma, J. Appl. Phys. 64 (1988) 6416–6423.
[9] K. Uestuener, M. Katter, W. Rodewald, IEEE Trans. Magn. 42 (2006) 2897–2899.
[10] M. Une, Y Sagawa, in: Proceedings of the 21st Workshop on Rare-Earth Permanent Magnets and their Applications, Bled, Slovenia, 2010.
[11] H. Sepehri-Amin, T. Ohkubo, M. Gruber, T. Schrefl, K. Hono, Scr. Mater. 89 (2014) 29–32.
[12] R.W. Lee, Appl. Phys. Lett. 46 (1985) 790–791.
[13] R. Lee, E. Brewer, N. Schaffel, IEEE Trans. Magn. 21 (1985) 1958–1963.
[14] K. Hioki, Sci. Technol. Adv. Mater. 22 (2021) 72–84.
[15] N. Yoshikawa, T. Iriyama, H. Yamada, Y. Kasai, V. Panchanathan, IEEE Trans. Magn. 35 (1999) 3268–3270.
[16] D.N. Brown, B. Smith, B.M. Ma, P. Campbell, IEEE Trans. Magn. 40 (2004) 2895–2897.
[17] J. Liu, H. Sepehri-Amin, T. Ohkubo, K. Hioki, A. Hattori, T. Schrefl, K. Hono, Acta Mater. 61 (2013) 5387–5399.
[18] K. Hioki, A. Hattori, T. Iriyama, J. Magn. Soc. Jpn. 38 (2014) 79–82.
[19] X. Zheng, M. Li, R. Chen, F. Lei, C. Jin, Z. Wang, J. Ju, W. Yin, D. Lee, A. Yan, Scr. Mater. 132 (2017) 49–52.
[20] Y. Liu, J. He, H. Yu, X. Zhong, Y. Liu, X. Li, Z. Liu, J. Magn. Magn. Mater. 516 (2020) 167339.
[21] T. Mouri, M. Kumano, H.Y. Yasuda, T. Nagase, R. Kato, Y. Nakazawa, H. Shimizu, Scr. Mater. 78–79 (2014) 37–40.
[22] J. Liu, H. Sepehri-Amin, T. Ohkubo, K. Hioki, A. Hattori, T. Schrefl, K. Hono, Acta Mater. 82 (2015) 336–343.
[23] T. Zhang, F. Chen, Y. Zheng, H. Wen, J. Wang, L. Zhang, L. Zhou, Intermetallics 73 (2016) 67–71.
[24] X. Tang, H. Sepehri-Amin, T. Ohkubo, K. Hioki, A. Hattori, K. Hono, Acta Mater. 123 (2017) 1–10.
[25] S. Soma, H. Shimizu, E. Shirado, S. Fujishiro, SAE Int. J. Altern. Powertrains 6 (2017) 1–8 2017-01–1221.
[26] L. Breiman, Mach. Learn. 45 (2001) 5–32.
[27] Pedregosa, et al., J. Mach. Learn. Res. 12 (2011) 2825–2830 https://scikit-learn.org/stable/modules/generated/sklearn.ensemble.RandomForestRegressor.html.
[28] B. Efron, The Jackknife, the Bootstrap and Other Resampling Plans, Society for Industrial and Applied Mathematics, 1982.
[29] D.R. Jones, M. Schonlau, W.J. Welch, J. Glob. Optim. 13 (1998) 455–492.
[30] Z. Wang, K. Pei, J. Zhang, R. Chen, W. Xia, J. Wang, M. Li, A. Yan, Acta Mater. 167 (2019) 103–111.
[31] V. Panchanathan, J. Mater. Eng. Perform. 4 (1995) 423–429.
[32] P. Yi, M. Lin, R. Chen, D. Lee, A. Yan, J. Alloy. Compd. 491 (2010) 605–609.
[33] A. Kirchner, D. Hinz, V. Panchanathan, O. Gutfleisch, K.-H. Muller, L. Schultz, K.H. Müller, L. Schultz, in: Proceedings of the INTERMAG Digest of Technical Papers. IEEE International Magnetics Conference, IEEE, 2000, p. 624.
[34] H. Sepehri-Amin, T. Ohkubo, S. Nagashima, M. Yano, T. Shoji, A. Kato, T. Schrefl, K. Hono, Acta Mater. 61 (2013) 6622–6634.
[35] H. Sepehri-Amin, D. Prabhu, M. Hayashi, T. Ohkubo, K. Hioki, A. Hattori, K. Hono, Scr. Mater. 68 (2013) 167–170.
[36] T. Akiya, J. Liu, H. Sepehri-Amin, T. Ohkubo, K. Hioki, A. Hattori, K. Hono, Scr. Mater. 81 (2014) 48–51.
[37] C. Jin, R. Chen, W. Yin, X. Tang, Z. Wang, D. Lee, A. Yan, IEEE Trans. Magn. 50 (2014) 1–4.
[38] H. Sepehri-Amin, L. Liu, T. Ohkubo, M. Yano, T. Shoji, A. Kato, T. Schrefl, K. Hono, Acta Mater. 99 (2015) 297–306.
[39] Z. Wang, J. Zhang, J. Wang, J. Ju, R. Chen, X. Tang, W. Yin, D. Lee, A. Yan, Acta Mater. 156 (2018) 136–145.